CRYSTAL GROWTH & DESIGN

pubs.acs.org/crystal

Article

Revealing the Nature of Defects in α-Ag_2WO_4 by Positron Annihilation Lifetime Spectroscopy: A Joint Experimental and Theoretical Study

Marcelo Assis,* Miguel Adolfo Ponce, Amanda Fernandes Gouveia, Daniele Souza, João Paulo de Campos da Costa, Vinícius Teodoro, Yara Galvão Gobato, Juan Andrés, Carlos Macchi, Alberto Somoza, and Elson Longo

Cite This: *Cryst. Growth Des.* 2021, 21, 1093−1102

Read Online

ACCESS | Metrics & More | Article Recommendations | Supporting Information

ABSTRACT: Electron−matter coupling is a fascinating way to tune and modify the properties of materials. In this work, we present a study on the formation and nature of vacancy-like defects in α-Ag_2WO_4 samples synthesized in a water or ethanol medium and subsequently submitted to electron beam irradiation at different exposure times. To understand the effects on the geometrical and electronic nature of the generated defects, the data obtained by positron annihilation lifetime spectroscopy were interpreted with the aid of first-principles calculations at the density functional theory level. To complement these results, X-ray diffraction, Raman spectroscopy, photoluminescence emissions, and field emission gun scanning electron microscopy techniques were also used. Based on the positron binding energy and the calculated and experimental positron lifetimes, the defect structure of the nonirradiated and irradiated samples was revealed. As a general feature, it was found that the defect structure is more complex for samples synthesized in ethanol than in water. In particular, the results show that all samples contain defects involving Ag vacancies and that the concentration of this type of defect increases with the irradiation time.

1. INTRODUCTION

The chemical and physical properties of semiconductors are largely determined by the population of defects, which have attracted continuous attention owing to their significant influence on such properties. Due to the similarity to enzymes, the domain where defects appear in the semiconductor structures can be considered active sites in which reactivity takes place and functionality occurs. At concentrations where defects do not interact with each other, they can be represented by individual electronic states isolated within the band of the host material, whose orbital and spin degrees of freedom can be controlled through the use of electromagnetic fields. However, there are still many challenges to be addressed, and further studies are necessary to unveil the nature and effects of the defects in semiconductors.[1−3]

In the field of solid materials, the ideal crystal formed by the periodic replication of unit cells does not exist. In reality, crystals are exposed to lattice vibrations, contain defects, and have surface and bulk vacancies, impurities, and non-stoichiometric compositions.[4−7] For scientists, the management of the presence of defects, which can be associated with a structural and electronic disorder, may enable the creation of new materials with unique, impossible physical properties for well-ordered crystal structures.[8−11] Understanding the nature of the defects and their formation and removal mechanisms in semiconductors constitutes a very challenging topic in materials science.[11−13]

Positron annihilation lifetime spectroscopy (PALS) is a well-recognized nondestructive nuclear technique to obtain specific information regarding structural and electronic aspects of open volume defects in solids.[14] The advantages of the use of PALS to study defects lie in the fact that positrons are prone to be localized and annihilated in sites with greater electronic density (i.e., more negative) than the average electronic density of the crystal lattice, allowing positron annihilation processes to take place in these sites, which act as positron traps with an associated specific open volume. In particular, PALS has demonstrated to be a powerful tool to investigate the presence of vacancy-like defects in semiconductors.[15,16] This technique has also been successfully used to obtain information on the defect structure of monocrystalline and polycrystalline semiconductor metal oxides.[17−24] In fact, vacancies in neutral or negative charge states act as efficient positron traps due to the reduced repulsion of positive ions, while positive vacancies do not trap positrons. On the other hand, it is well documented that multiple vacancies or vacancy clusters are even more effective positron traps than single vacancies. In this case, the

Received: October 15, 2020
Revised: January 13, 2021
Published: January 25, 2021

https://dx.doi.org/10.1021/acs.cgd.0c01417
Cryst. Growth Des. 2021, 21, 1093−1102

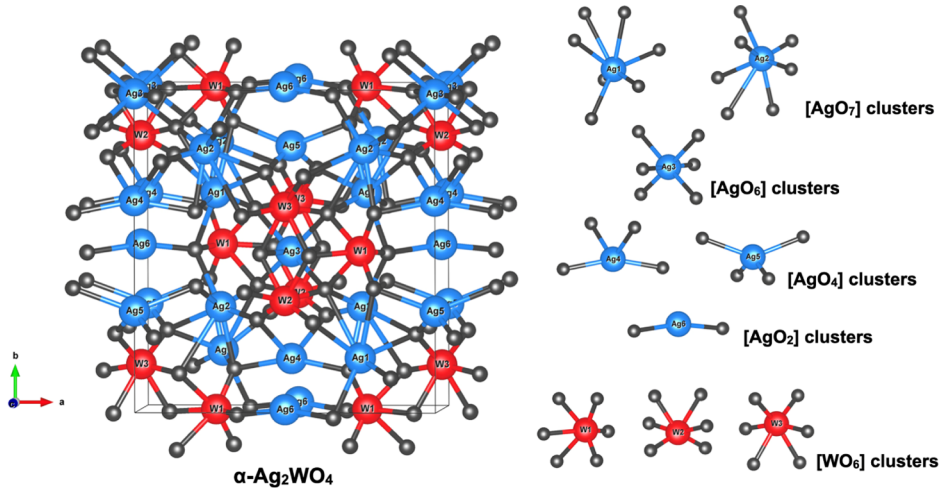

Figure 1. Orthorhombic α-Ag_2WO_4 structure and the representation of the $[AgO_x]$ (x = 2, 4, 6, and 7) and $[WO_6]$ clusters. W atoms are represented in red, Ag atoms in blue, and O atoms in dark gray.

charge-state dependence is the same as that described for vacancies. Every time an open volume exists in a defect complex, it appears for the positron as a vacancy-like defect, that is, if a negative ion is bound to a vacancy, this defect appears as an effective positron trap. It must be said that the effectiveness of this trap depends on the total charge of the vacancy complex. Under this frame, a neutral pair consisting of a negative ion and a positive vacancy also acts as an effective positron trap with the positron localized inside the vacancy.[25]

There has been a growing interest in silver tungstate (α-Ag_2WO_4) due to its unique properties with a wide range of applications in the field of environmental remediation, photocatalysis, etc.[26] The three-dimensional (3D) structure of the orthorhombic α-Ag_2WO_4 is displayed in Figure 1. Their crystal lattice is composed of distorted $[WO_6]$ and $[AgO_x]$ (x = 2, 4, 6, and 7) clusters acting as lattice building blocks.

This complex structure is responsible for a wide range of technological applications. From an electronic point of view, the top of the valence band (VB) consists of unique hybridized Ag 4d and O 2p orbitals, which can leave the top position of the VB and narrow down the band gap. The bottom of the conduction band (CB) composed of delocalized s and/or p orbitals presents significant dispersity, which means that it possesses high migration efficiency of photogenerated electrons.[27−29]

With the substantial developments of electron microscopes and their beam sources, the use of transmission electron microscopes is no more limited to material characterization. Recently, different research studies have focused on the effect of electron beam irradiation (EBI) on the generation of defects since more and more related applications have been unveiled.[30−38] Under EBI, energy is transferred from energetic electrons to both electrons and atomic nuclei in the target materials. In this context, our research group has demonstrated that EBI on materials could be employed for advanced fabrication, modification, and functionalization of α-Ag_2WO_4. Its enhanced performance is strongly dependent on the large anisotropy produced by the complex structure of the α-Ag_2WO_4 oxide, which leads to the generation of defects.[27,29,39−55] Therefore, it is necessary to have a deep knowledge of the structure, nature, and concentration of defects at nanometric and sub-nanometric scales resulting from the α-Ag_2WO_4 material modification due to EBI for a rational optimization of their properties and the search for new applications. To the best of our knowledge, a systematic investigation on the type of defects and their nature in α-Ag_2WO_4 provoked by EBI has not been conducted yet.

The main goals of this work are twofold: (i) to gain a deeper understanding of the formation process and nature of atomic defects in α-Ag_2WO_4 under EBI as a function of the solvent used for the synthesis of the samples, that is, water (WT) and ethanol (AL). The experimental information on these defects was obtained using PALS as well as X-ray diffraction (XRD) with Rietveld refinements, Raman spectroscopy, photoluminescence (PL) emissions, and field emission gun scanning electron microscopy (FEG-SEM) and (ii) to understand the fine effects of the geometrical and electronic nature of the generated defects. For this purpose, first-principles calculations at the density functional theory (DFT) level were performed to complement and rationalize the experimental PALS results.

This paper contains additional three sections. In the Experimental Section, we report the sample synthesis and characterization as well as the computational methods and model systems employed. In Section 3, we present and discuss the obtained results. Finally, the conclusions are summarized in the final Section.

2. EXPERIMENTAL SECTION

2.1. Synthesis. The synthesis of α-Ag_2WO_4 samples was performed by the co-precipitation (CP) method in water (WT) and ethanol (AL) media at 70 °C. The details and reagents used followed the description made by de Foggi et al.[45] α-Ag_2WO_4 semiconductor powder was cold-pressed at a pressure of ∼500 MPa into circular pellets with 5 mm in diameter and ∼1 mm in thickness.

2.2. EBI. To obtain the materials irradiated with electrons, the pellet α-Ag_2WO_4 samples were placed in a field emission gun scanning electron microscope, model Supra 35-VP (Carl Zeiss, Germany), with an acceleration voltage of 30 kV for 3 (WT3, AL3), 6 (WT6, AL6), and 9 (WT9, AL9) min.

2.3. Characterization. The α-Ag_2WO_4 samples were structurally characterized by XRD using a D/Max-2500PC diffractometer (Rigaku, Japan) with Cu Kα radiation (λ = 1.5406 Å) in the 2θ range between 10−110°, at a scan speed of 1° min^{-1} in the Rietveld routine. The Rietveld refinements were performed in the General Structure Analysis System (GSAS) program. Micro-Raman spectra were recorded using the iHR550 spectrometer (Horiba Jobin-Yvon, Japan) equipped with a charge-coupled device (CCD) detector and

https://dx.doi.org/10.1021/acs.cgd.0c01417
Cryst. Growth Des. 2021, 21, 1093−1102

an argon-ion laser (Melles Griot) operating at 514.5 nm with a maximum power of 200 mW and a fiber microscope. The morphologies, textures, and sizes of the samples obtained were observed with a field emission gun scanning electron microscope (Supra 35-VP, Carl Zeiss, Germany) operated at 10 kV. PL measurements were performed at room temperature (RT) using a 500M Spex spectrometer coupled to a GaAs PMT. A Kimmon He−Cd laser (325 nm line) with laser power up to 40 mW was used as the excitation source.

2.4. PALS. PALS spectra were recorded using a fast−fast spectrometer with a time resolution of 251 ps in a collinear geometry. A 10 μCi-sealed source of ^{22}NaCl deposited onto two thin Kapton foils (7.5 μm thick) sandwiched between two identical samples was used as a positron source. The spectra were recorded at RT, and typical 1.5−2 × 10^6 counts per spectrum were collected. The lifetime values reported in this work for each sample are at least an average of 10 measurements in the same experimental conditions. After subtracting the background and the source contribution, the PALS spectra were analyzed using the LT10 program.[56]

2.5. Computational Methods and Model Systems. First-principles calculations at the DFT level were carried out using the Viena *ab initio* simulation package (VASP) version 5.4.4.[57,58] The semilocal Perdew−Burke−Ernzerhof[59] exchange and the correlation energy functional within the spin-polarized generalized gradient approximation (GGA) formulation were employed. The Kohn−Sham equations were solved using the projector-augmented wave (PAW) method,[60] employing the following projectors: Ag ($4d^{10}$,$5s^1$), W ($5p^6$,$5d^4$,$6s^2$), and O ($2s^2$,$2p^4$), where the numbers in parentheses represent the valence states. In the calculation, a Gaussian smearing of 0.01 eV was used, and the atoms were allowed to relax until all forces were smaller than 0.01 eV/A on every atom and the equilibrium volume of crystals was obtained by the minimization of stress tensor through a plane-wave cutoff of 834 eV and another of 469 eV to optimize the atomic force. For the Brillouin zone integration, a *k*-mesh of 1 × 1 × 2 for the stress tensor and atomic force optimizations were employed.

To obtain the theoretical positron lifetimes (τ) for the bulk and vacancy states in the α-Ag_2WO_4 structure, calculations were performed according to Macchi et al.[61] The positron parameters were calculated using DFT within the so-called standard scheme.[62] The positron wave functions and the parameters τ and the positron binding energy (E_b) were obtained through the Doppler program included in the MIKA package,[63] considering as an input parameter the electron density calculated by VASP.

The positron binding energy is defined as the difference between the ground energy (E_0) of the delocalized positron and the energy of the positron trapped in the considered defect (E_d)

$$E_b = E_0 - E_d \quad (1)$$

This energy indicates the energy gained for a positron trapped in a specific defect. A positive sign for E_b indicates that the considered defect acts as a positron trapping center.

To get positron parameters, it is necessary to calculate the electron−positron correlation potential. To this end, the local density approximation (LDA) was considered by employing the parameterization proposed by Boroński and Nieminen.[64] Such parameterization was corrected to take into account the incomplete positron screening,[62] in which the value of the high-frequency dielectric constant was measured as follows: *ad-hoc* (ε_∞ = 17.6).

To model the orthorhombic α-Ag_2WO_4 structure, we used the relaxed cell previously described.[65] A supercell of 672 atoms (2 × 2 × 3 repetitions of the relaxed cell) was used to calculate the positron lifetimes in the different defect states, considering different supercells containing (i) an oxygen monovacancy (V_O); (ii) a tungsten monovacancy (V_W); (iii) a silver monovacancy (V_{Ag}); (iv) a divacancy constituted by silver and oxygen (V_{Ag} + V_O); (v) a trivacancy formed by one silver vacancy and two oxygen vacancies (V_{Ag} + $2V_O$); and finally, a hexavacancy containing two silver and four oxygen vacancies ($2V_{Ag}$ + $4V_O$). In this work, different oxygen vacancies were modeled by removing an O atom from the different clusters that are the building blocks of the α-Ag_2WO_4 crystal structure ([WO_6] and [AgO_x] (x = 2, 4, 6, and 7) clusters). The V_W was created by removing a W atom from the [WO_6] cluster located near the center of the supercell. In the case of four nonequivalent V_{Ag} belonging to the different [AgO_x] clusters (x = 2, 4, 6, and 7), an Ag atom at each of the four possible [AgO_x] clusters was removed. Additionally, for each V_{Ag}, different vacancies were modeled by removing one or two oxygen atoms that are the nearest neighbors to each V_{Ag} to form a divacancy or a trivacancy (V_{Ag} + V_O and V_{Ag} + $3V_O$, respectively). To form a hexavacancy, two adjacent trivacancies (V_{Ag} + $2V_O$) were considered.

As a first approach, a further relaxation of the defective structures was not taken into account for all calculations. Besides, all defect states were considered in their neutral states. It is worth mentioning that for different semiconductors the calculated positron lifetimes for defects in the negative charge states are always slightly shorter (between ∼2 and ∼8%, depending on the considered negative charge state) than those determined for the same semiconductor containing defects in its neutral states.[66,67]

3. RESULTS AND DISCUSSION

3.1. X-ray Diffraction. XRD analysis was performed to understand the structural order/disorder of the materials at long range (periodicity and organization) in relation to the solvent (WT and AL) used and its subsequent modification by EBI. Figure SI-1 (see the Supporting Information) shows the corresponding XRD patterns. According to the analysis of the results, all samples correspond to α-Ag_2WO_4 with an orthorhombic structure and a *Pn2n* space group, which is in accordance with the crystallographic record no. 248969[68] in the Inorganic Crystal Structure Database (ICSD). All samples have well-defined peaks, which are associated with a high degree of long-range order. No additional peaks were observed, demonstrating that the pure α-Ag_2WO_4 phase was obtained in both solvents and also after modification by EBI.

The lattice parameters (a, b, and c) as well as the cell volume (v), full width at half-maximum (FWHM), and reliability parameters (R_{wp}, R_p, χ^2) were obtained by Rietveld refinements and are shown in Figure SI-2 and Table SI-1. The reliability parameters obtained in the Rietveld refinement indicate that the results have a high degree of quality. It was observed that for the samples synthesized in WT or AL and subjected to EBI, there was an increase in the values of the lattice parameters and unit cell volume. These changes can be directly related to the FWHM of the main α-Ag_2WO_4 diffraction peak (231) at 2θ = 32°. According to Table SI-1, the FWHM increases with the EBI time, causing the appearance of a more disordered system.[39]

3.2. Micro-Raman Spectroscopy. According to our group's theory, the orthorhombic α-Ag_2WO_4 structure belongs to the C_{2v}^{10} symmetry group, which has 21 active Raman modes from the decomposition point Γ = ($6A_{1g}$ + $5A_{2g}$ + $5B_{1g}$ + $5B_{2g}$). Although all 21 modes are active in Raman, in this case, only nine of them can be observed (see Figure SI-3) due to the overlapping of some modes as well as the high degree of disorder of the systems at short range. Previous results[44] point out that the vibrational modes located at 106 and 317 cm^{-1} are related to [AgO_x] clusters (x = 2, 4, 6, and 7), while the vibrational modes located between 600 and 1000 cm^{-1} refer to the O−W−O bending angles and W−O stretching bonds of the [WO_6] clusters.[28]

3.3. Field Emission Gun Scanning Electron Microscopy. The morphologies, particle sizes, and textures of all prepared pellet samples of α-Ag_2WO_4 (WT and AL) were investigated by FEG-SEM, and the results are presented in

https://dx.doi.org/10.1021/acs.cgd.0c01417
Cryst. Growth Des. 2021, 21, 1093−1102

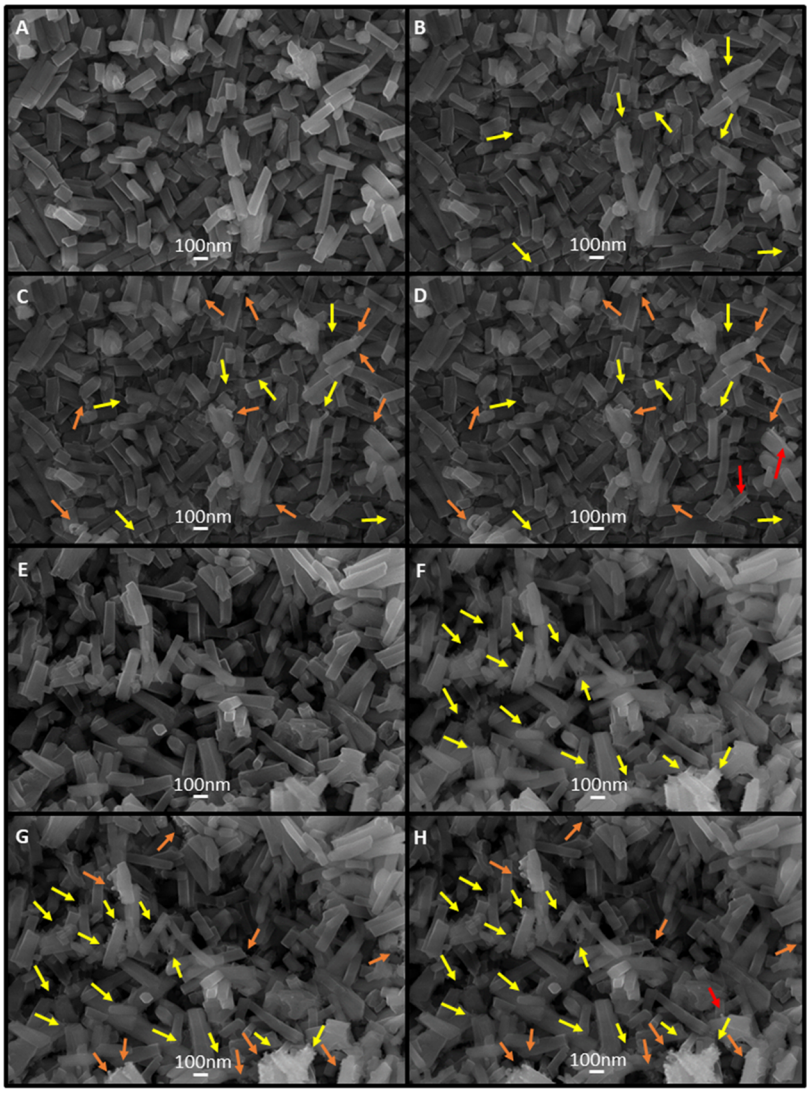

Figure 2. FEG-SEM of WT samples irradiated for (A) 0 min, (B) 3 min, (C) 6 min, and (D) 9 min and AL samples irradiated for (E) 0 min, (F) 3 min, (G) 6 min, and (H) 9 min.

Figure SI-4. It was observed that both WT (Figure SI-4A) and AL (Figure SI-4B) samples have a rodlike morphology with a hexagonal shape and (001), (010), and (101) exposed surfaces. From the analysis of the results (see Figure SI-5), the average length and width of the rods of the WT sample are 0.37 ± 0.13 and 0.13 ± 0.10 μm, respectively, while for the AL sample, the corresponding values are 0.66 ± 0.17 and 0.27 ± 0.13 μm.

Figure 2 shows the behavior of the WT (Figure 2A−D) and AL (Figure 2E−H) pellets under EBI at a voltage of 30 kV for 0, 3, 6, and 9 min. We noted that the exposure to the electron beam generates the delocalized growth of some metallic Ag particles on the surface of α-Ag_2WO_4. This phenomenon was reported in previous studies, and it is due to the reduction of the Ag^+ cation at both $[AgO_2]$ and $[AgO_4]$ clusters, thus generating Ag metal nanoparticles on the semiconductor surface.[28,29,46,48,50,69,70]

3.4. Photoluminescence. PL measurements provide important information about the structural defects in the crystal lattice. Figure SI-6 exhibits the PL spectra of α-Ag_2WO_4 samples at room temperature with laser excitation at 325 nm. The behavior of the PL spectra is associated with multiphonon processes, where the relaxation of electron momentum occurs by several paths with the participation of various energy intermediate states within the forbidden band-gap region.[71−73] The spectra arise from the octahedral $[WO_6]$ and $[AgO_x]$ (x = 2, 4, 6, and 7) clusters, with maximum emission centered in the blue-green region at 449 nm.[28,45,65,74] The luminescence mechanism of these materials is assigned to the charge transfer within the $[WO_6]$ clusters, from the 2p orbital of the O atom and the 4d orbital of the Ag atom of the VB to the 5d orbital of the W atom of the CB. Moreover, it is known that a modified crystal lattice, i.e., a lattice with increased structural defect density, also favors the emission in the blue-green region, which is more energetic.[28,75] In particular, the PL emissions can be associated with the electronic transitions from the $^1A_1$ ground state to the $^1T_2$ excited state corresponding to the octahedral $[WO_6]$ cluster.[73,76] To understand the PL behavior of all samples, the PL spectra were deconvoluted to investigate the contributions of the individual components using a Voigt function and considering the peak positions and their respective areas, as seen in Figure SI-6. For all samples, the spectra were decomposed into two components centered at 450 and 490 nm, contributing to the blue and green colors of the visible spectrum, respectively (see Figure 3).

https://dx.doi.org/10.1021/acs.cgd.0c01417
Cryst. Growth Des. 2021, 21, 1093−1102

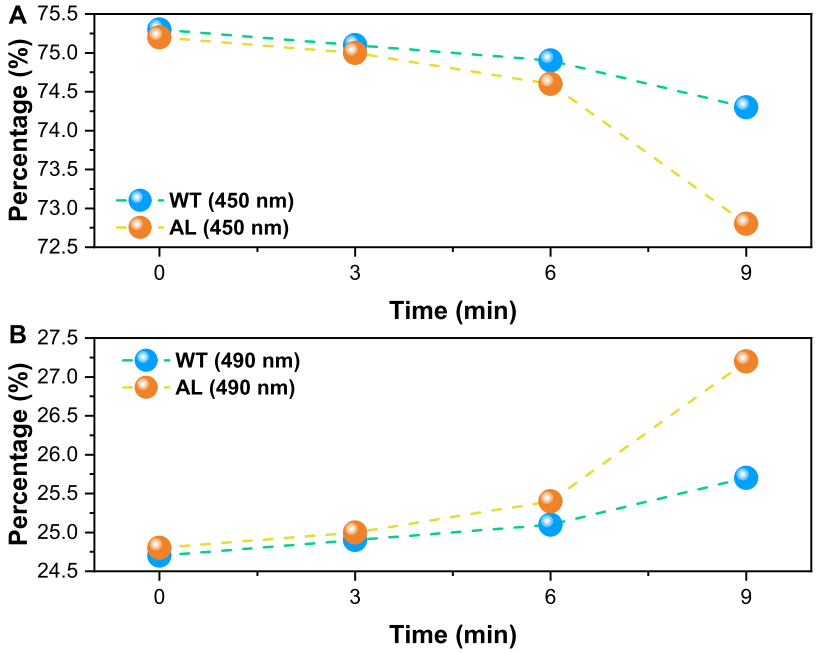

Figure 3. Percentages of PL deconvolution components for samples located at (A) 450 nm and (B) 490 nm as a function of EBI time.

After the deconvolution process, the contribution of the band centered at 450 nm slightly decreases, while the band centered at 490 nm increases. This can be related to structural defects (shallow defects) of the band located at shorter wavelengths and vacancy defects (deep defects) of the band at longer wavelengths, revealing an increase in the number of vacancies as a function of EBI exposure time. Besides that, it was observed that the increased number of defects is more pronounced in the AL than in the WT-synthesized samples.

3.5. PALS Measurements. From the spectra decomposition, several lifetime components could be obtained, each of them characterized by a lifetime τ_i and having an associated intensity I_i. The state i can be delocalized in the crystal lattice (bulk state), or localized at different defect sites in which positrons become trapped and annihilated. In this last case, the value of the positron lifetime reflects the size of the open volume associated with the defect in which positrons are annihilated. Increased lifetime values indicate that positrons become trapped in bigger open volumes.

All PALS spectra obtained in this work were satisfactorily fitted considering three lifetime components. Initially, a free constraint fitting analysis showed the presence of an almost constant long-lived lifetime, τ_3 = 1800 ± 100 ps, usually assigned to the *ortho*-positronium (*o*-Ps) annihilation via the pick-off process. Then, a second analysis was carried out fixing this component at 1800 ps. As a result, a small value of intensity associated with τ_3 (I_3 < 2%) was obtained, indicating that the powder compression process used to fabricate the pellets was good enough to produce well-compacted samples. It is worth mentioning that this long lifetime component related to the small value of I_3 was not considered for further discussions. I_1 and I_2 were then normalized to 100%.

On the other hand, α-Ag_2WO_4 microcrystals present a particle size higher than the typical positron diffusion length, $L_+ \sim 100$ nm, in solids.[14] In this scenario, it was assumed that almost all positrons are annihilating in defects located inside the grains (i.e., intragranular defects). Values of the positron lifetime parameters obtained from the decomposition of the PALS spectra recorded on samples synthesized in WT and AL solvents are reported in Tables 1 and 2, respectively.

Table 1. Values of Positron Lifetimes and Their Associated Intensities Obtained from the Decomposition of PALS Spectra of α-Ag_2WO_4 Microcrystalline WT Samples Nonirradiated and Irradiated at Different Times

irradiation time (min)	τ_1 (ps)	I_1 (%)	τ_2 (ps)	I_2 (%)
0	172 ± 1	24.7 ± 0.5	274 ± 2	72.6 ± 0.5
3	156 ± 3	24.9 ± 0.5	274 ± 2	75.1 ± 0.5
6	154 ± 2	21.0 ± 0.5	271 ± 1	79.0 ± 0.5
9	141 ± 1	20.0 ± 0.5	263 ± 1	80.0 ± 0.5

Table 2. Values of Positron Lifetimes and Their Associated Intensities Obtained from the Decomposition of PALS Spectra of α-Ag_2WO_4 Microcrystalline AL Samples Nonirradiated and Irradiated at Different Times

irradiation time (min)	τ_1 (ps)	I_1 (%)	τ_2 (ps)	I_2 (%)
0	222 ± 1	61.4 ± 0.5	345 ± 2	38.6 ± 0.5
3	214 ± 1	50.8 ± 0.5	324 ± 2	49.2 ± 0.5
6	204 ± 1	39.0 ± 0.5	299 ± 1	61.0 ± 0.5
9	183 ± 1	24.8 ± 0.5	286 ± 1	75.2 ± 0.5

It is important to note that the reported values of the positron lifetime, $\overline{\tau}$, and intensity, $\overline{I}$, in Tables 1 and 2 are the result of averaging the decomposition of approximately 15 consecutive PALS spectra in the same experimental conditions. The associated errors presented in these tables correspond to the standard error of both mean measurements. According to Peters,[77] the standard error of the mean of a set of measurements, for example, a set of 15 positron lifetimes values, is defined as follows

https://dx.doi.org/10.1021/acs.cgd.0c01417
Cryst. Growth Des. 2021, 21, 1093−1102

$$s_\tau = \left(\frac{\sum_{i=1}^{15}(\tau_i - \tau)^2}{15 - 1}\right)\left(\frac{1}{\sqrt{15}}\right) \quad (2)$$

where the first term of the expression corresponds to the standard deviation of the mean positron lifetime and the second term is related to the size of the set. Clearly, when the number of observations is large, the uncertainty in the estimate of the mean positron lifetime can be small. Similarly, this formula can be used to calculate the standard error of the mean intensity $S_{\bar{I}}$. Applying this formula to the obtained sets of positron lifetimes and intensities, we estimated standard errors $S_{\bar{\tau}}$ and $S_{\bar{I}}$ of about 1 ps and 0.5%, respectively.

First-principles calculations are extremely useful for the interpretation and rationalization of the experimental results of PALS measurements. The calculated positron lifetimes and the corresponding binding energies of the supercell containing different vacancy-like defects are presented in Table 3.

Table 3. Values of Positron Lifetimes, τ, and Binding Energy, E_b, for Different Positron Defect States in the α-Ag_2WO_4 Structure

cluster	defect state	τ (ps)	E_b (eV)
bulk		172	
$[WO_6]$, $[AgO_x]$ (x = 2, 4, 6, and 7)	V_O	173	~0
$[WO_6]$	V_W	178	0.1
$[AgO_2]$	V_{Ag}	230	0.6
	$V_{Ag} + V_O$	255	0.8
	$V_{Ag} + 2V_O$	275	1.0
$[AgO_4]$	V_{Ag}	225	0.6
	$V_{Ag} + V_O$	250	0.8
	$V_{Ag} + 2V_O$	265	0.9
$[AgO_6]$	V_{Ag}	204	0.4
	$V_{Ag} + V_O$	223	0.5
	$V_{Ag} + 2V_O$	239	0.7
$[AgO_7]$	V_{Ag}	227	0.6
	$V_{Ag} + V_O$	250	0.8
	$V_{Ag} + 2V_O$	264	0.9
	$2V_{Ag} + 4V_O$	311	1.2

From the analysis of the calculated E_b values reported in Table 3, we can infer that independently of the type of cluster from which one oxygen atom was extracted, V_O can hardly trap positrons even in its neutral charge state. This behavior is due to the delocalization of the positron wave function. This effect can be seen in Figure 4A, where it is possible to visualize a positron wave function isodensity plot calculated for V_O created between two clusters (one $[WO_6]$ and one $[AgO_4]$). On the contrary, cation vacancies such as V_W and V_{Ag} act as effective positron traps, which is in good agreement with the results reported in the literature for semiconducting oxides.[15,17,18] The cationic vacancy V_W is not a deep positron trap since its binding energy is small when compared to that calculated for V_{Ag} in different cluster structures, that is, ~0.1 eV versus ~0.6 eV. In Table 3, it can also be seen that the positron lifetime for V_W = 178 ps is barely 4% higher than that calculated for the α-Ag_2WO_4 bulk of the supercell (τ_b = 172 ps). This behavior can be attributed to a weak localization of the positron wave function in the defect, according to the isodensity plot in Figure 4B. As observed, the positron wave function is mostly localized in the interstitial space near the missing W atom. In the case of the cationic vacancy V_{Ag},

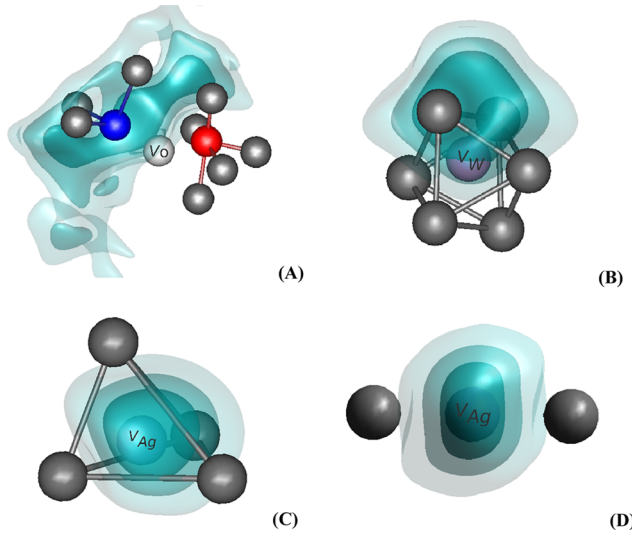

Figure 4. Positron wave function isodensities calculated for monovacancy states: (A) V_O created between one $[WO_6]$ and one $[AgO_4]$ cluster; (B) V_W created inside a $[WO_6]$ cluster; (C) V_{Ag} formed inside a $[AgO_4]$ cluster; and (D) V_{Ag} created within a $[AgO_2]$ cluster. The positron isodensities are represented by three surface contours, which correspond to 70, 50, and 30% of the maximum positron density. For the sake of clarity, only the participating clusters are shown in the figures. W atoms are represented in red, Ag atoms in blue, and O atoms in dark gray. Missing atoms related to the different monovacancies are labeled.

remarkable changes in the calculated positron parameters are not sensed, except for the V_{Ag} at the $[AgO_6]$ cluster. In particular, when an Ag atom is extracted from a $[AgO_2]$ cluster, there is a strong increase in the positron lifetime with respect to τ_b, resulting in a calculated positron lifetime approximately 33% higher than τ_b and a positron binding energy of 0.6 eV. If V_{Ag} occurs at the $[AgO_7]$ or $[AgO_4]$ cluster, the corresponding τ and E_b values are slightly smaller than those obtained for the same vacancy created in a $[AgO_2]$ cluster. Conversely, for a V_{Ag} created in a $[AgO_6]$ cluster, more significant changes in the positron parameters can be obtained, which are reflected in a strong localization of the positron wave function within the empty space left by the missing Ag atom. As an example, Figures 4C and 3D display positron wave function isodensity plots calculated for the monovacancy states characteristic of a V_{Ag} created inside $[AgO_4]$ and $[AgO_2]$ clusters, respectively.

On the other hand, when oxygen vacancies are aggregated to a V_{Ag} to form different Ag−O vacancy complexes (i.e., one V_{Ag} complex with one or more oxygen vacancies), the related positron lifetimes are higher than those calculated for the positron annihilated in a V_{Ag} (~10 and ~20% for a Ag−O divacancy and a Ag−O trivacancy, respectively), meaning that these complexes are deeper positron traps. Figure 5A−C displays positron wave function isodensity plots calculated for the vacancy complexes representing a $V_{Ag} + V_O$ divacancy created inside a $[AgO_2]$ cluster, a $V_{Ag} + 2V_O$ trivacancy corresponding to the whole missing $[AgO_2]$ cluster, and a $V_{Ag} + 2V_O$ trivacancy formed inside a $[AgO_4]$ cluster, respectively. In the case of V_{Ag}, the positron wave function is strongly localized inside the Ag vacancy and the corresponding positron wave function isodensities are slightly affected by the presence of V_O. Finally, important changes in the positron parameters regarding the $2V_{Ag} + 4V_O$ hexavacancy were observed. We could note that the presence of a second d V_{Ag} reduces the

https://dx.doi.org/10.1021/acs.cgd.0c01417
Cryst. Growth Des. 2021, 21, 1093−1102

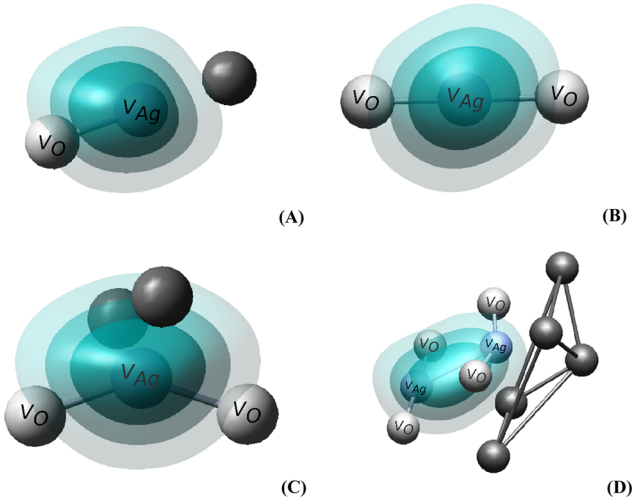

Figure 5. Positron wave function isodensities calculated for vacancy complexes: (A) $V_{Ag} + V_O$ divacancy created inside a $[AgO_2]$ cluster; (B) $V_{Ag} + 2V_O$ trivacancy corresponding to the whole missing $[AgO_2]$ cluster; (C) $V_{Ag} + 2V_O$ trivacancy formed inside a $[AgO_4]$ cluster; and (D) $2V_{Ag} + 4V_O$ hexavacancy created between a $[AgO_2]$ cluster and a neighboring $[AgO_7]$ cluster. The positron isodensities are represented by three surface contours, which correspond to 70, 50, and 30% of the maximum positron density within the contour. For the sake of clarity, only the participating clusters are shown in the figures. Ag atoms are shown in blue and O atoms in dark gray. Missing atoms related to the different monovacancies forming the vacancy complexes are labeled.

positron lifetime and the corresponding E_b values, strongly modifying the positron wave function, according to the isodensity plot presented in Figure 5D, where it is possible to see the positron localized between two Ag vacancies.

Based on the lifetime values obtained by first-principles calculations, the experimental results reported in Tables 1 and 2 can be rationalized as follows.

3.5.1. For the WT samples. The shortest lifetime τ_1 is always lower than the calculated τ_b. In such a case, τ_1 must be considered a reduced bulk lifetime due to positron annihilation in intragranular defects characterized by the second lifetime component. Therefore, the relevant information linked to vacancy-like defects can be obtained from τ_2 and I_2. For the nonirradiated sample, $\tau_2 = 274 \pm 2$ ps and $I_2 \sim 73\%$. Taking into account the calculated positron lifetimes reported in Table 3, the experimental τ_2 value can be interpreted as the result of positron annihilations in Ag−O vacancy complexes. Specifically, positron traps have a size distribution around a mean value equivalent to that formed by two oxygen vacancies surrounding one silver vacancy ($V_{Ag} + 2V_O$). Besides, the elevated I_2 value indicates a high concentration of this kind of defect in the nonirradiated sample. When the EBI exposure time increases, the τ_2 values decrease from 274 to 263 ps, while the associated I_2 values increase from ∼73 to ∼80%. The change in the positron lifetime can be assigned to a progressive decrease in the concentration of Ag−O vacancy complexes (greater than $V_{Ag} + 2V_O$) with a consequent increase in the concentration of a smaller type of vacancies such as V_{Ag} and $V_{Ag} + V_O$. It is worth mentioning that the I_2 increases reflect an increment of the total concentration of defects related to silver vacancies.

3.5.2. For the AL Samples. The interpretation of the experimental positron lifetimes reported in Table 2 requires a different sequence when compared with the results obtained for the irradiated and nonirradiated WT samples. First, all τ_2 and I_2 values are respectively higher and lower than those obtained for the WT samples. Regarding the τ_2 experimental value, it is higher than the maximum theoretical lifetime calculated for the different defect states listed in Table 3. As a consequence, it must be assumed that positrons are annihilated in vacancy complexes (VC) containing Ag vacancies (Ag-VC) with an associated open volume larger than that of a $2V_{Ag} + 4V_O$ hexavacancy. To obtain higher theoretical positron lifetimes, it is necessary to build more complex structures of vacancy clusters that should be associated with real defects. For our calculations, we tried to avoid building defects that could hardly be interpreted in terms of a feasible defect structure. On the other hand, increased EBI exposure times decrease the systematic τ_2, which in turn is correlated with a strong increase of I_2. This behavior could be interpreted as a progressive decrease in the VC concentration with a consequent increase in the concentration of Ag−O vacancy complexes having an equivalent mean size between a $V_{Ag} + 2V_O$ trivacancy and a $2V_{Ag} + 4V_O$ hexavacancy. As it can be seen in Table 2, when the irradiation times increase, the τ_1 and I_1 values systematically decrease from ∼219 to ∼178 ps and from ∼61 to ∼25%, respectively.

To simplify the interpretation of the PALS results obtained for the AL samples, the data obtained by measuring the samples submitted to the maximum EBI time (9 min) are first presented and discussed. At this irradiation time, the experimental τ_1 value is, within the error bars, equal to the calculated lifetime τ_b, and its associated intensity is non-negligible ($I_1 \sim 25\%$). Consequently, it can be concluded that a shorter lifetime is an average positron lifetime, resulting from the contributions of the reduced bulk positron lifetime and those coming from positron annihilations in V_{Ag}. Thus, in terms of the theoretical positron lifetimes reported in Table 3, by decreasing the EBI exposure times the τ_1 tends to increase, which can be mainly assigned to a significant and systematic increase in positron annihilability in V_{Ag}.

4. CONCLUSIONS

Information on the type and concentration of defects and the localization of their electronic levels in the semiconductor oxides is critical to design materials with specific characteristics to be used in different technological applications. In particular, it is essential to understand the changes in the structural defects at nanometric and sub- nanometric scales as a consequence of the modification of materials due to EBI.

A detailed analysis based on the results obtained by PALS together with the theoretical positron lifetime values calculated using first-principles calculations at the DFT level made it possible to establish the nature of vacancy-like defects in both pure α-Ag_2WO_4 samples and those submitted to EBI. The PL measurements revealed that the increase of EBI exposure time induces a progressive change in the defect structure from shallow vacancy defects to deep ones.

The main conclusions of this work can be summarized as follows: (i) For nonirradiated α-Ag_2WO_4 samples synthesized in water, the defects are mainly composed of a high concentration of Ag−O vacancy complexes with a mean size equivalent to a trivacancy formed by two V_O surrounding one Ag vacancy. (ii) The defects in the nonirradiated α-Ag_2WO_4 samples synthesized in ethanol mainly comprise a Ag vacancy complemented with a non-negligible concentration of vacancy clusters containing three or more V_{Ag}. (iii) In the irradiated

https://dx.doi.org/10.1021/acs.cgd.0c01417
Cryst. Growth Des. 2021, 21, 1093−1102

samples synthesized in water, we observed that an increase of the EBI exposure times causes a larger progressive decrease in the concentration of Ag−O vacancy complexes than a trivacancy with a concomitant increase in the concentration of V_{Ag} and Ag−O divacancies. In addition, a slight increase in the total concentration of defects related to V_{Ag} was detected. In these samples, the irradiation induced the formation of new small Ag-related defects. Finally, (iv) for the irradiated samples synthesized in ethanol, the increase of irradiation times induces a progressive decrease in the concentration of vacancy clusters containing Ag vacancies with concomitant formation of an important number of Ag−O vacancy complexes bigger than a V_{Ag} + $2V_O$ trivacancy.

The present results have provided a complete defect structural description of pure α-Ag_2WO_4 semiconductor under EBI that would contribute to the better control of its tunable response. It is not only related to the formation of quantum dots, which confine the electrons at the Ag vacancy centers, but also provides unambiguous physical meaning on the nature of defects generated by EBI. The knowledge gained by this study can allow engineers to incorporate new functionalities into Ag_2WO_4-based semiconductor devices.

■ ASSOCIATED CONTENT

Supporting Information

The Supporting Information is available free of charge at https://pubs.acs.org/doi/10.1021/acs.cgd.0c01417.

XRD, Rietveld refinements, Raman spectra, FE-SEM images, and photoluminescence deconvolution (PDF)

■ AUTHOR INFORMATION

Corresponding Author

Marcelo Assis − *CDMF, LIEC, Chemistry Department, Federal University of São Carlos - (UFSCar), 13565-905 São Carlos, SP, Brazil;* orcid.org/0000-0003-0355-5565; Email: marcelostassis@gmail.com

Authors

Miguel Adolfo Ponce − *Institute of Materials Science and Technology (INTEMA), Mar del Plata 7600, Argentina*

Amanda Fernandes Gouveia − *Institute of Chemistry, State University of Campinas, 13083-970 Campinas, SP, Brazil; Department of Physical and Analytical Chemistry, University Jaume I (UJI), Castelló 12071, Spain;* orcid.org/0000-0003-3441-3674

Daniele Souza − *Physics Department - Federal University of São Carlos (UFSCar), 13565-905 São Carlos, SP, Brazil*

João Paulo de Campos da Costa − *CDMF, LIEC, Chemistry Department, Federal University of São Carlos - (UFSCar), 13565-905 São Carlos, SP, Brazil;* orcid.org/0000-0002-7366-6829

Vinícius Teodoro − *CDMF, LIEC, Chemistry Department, Federal University of São Carlos - (UFSCar), 13565-905 São Carlos, SP, Brazil*

Yara Galvão Gobato − *Physics Department - Federal University of São Carlos (UFSCar), 13565-905 São Carlos, SP, Brazil;* orcid.org/0000-0003-2251-0426

Juan Andrés − *Department of Physical and Analytical Chemistry, University Jaume I (UJI), Castelló 12071, Spain;* orcid.org/0000-0003-0232-3957

Carlos Macchi − *CIFICEN (UNCPBA-CICPBA-CONICET) and Instituto de Física de Materiales Tandil (UNCPBA), B7000GHG Tandil, Argentina*

Alberto Somoza − *CIFICEN (UNCPBA-CICPBA-CONICET) and Instituto de Física de Materiales Tandil (UNCPBA), B7000GHG Tandil, Argentina*

Elson Longo − *CDMF, LIEC, Chemistry Department, Federal University of São Carlos - (UFSCar), 13565-905 São Carlos, SP, Brazil;* orcid.org/0000-0001-8062-7791

Complete contact information is available at: https://pubs.acs.org/10.1021/acs.cgd.0c01417

Notes

The authors declare no competing financial interest.

■ ACKNOWLEDGMENTS

This work was partly funded by the Fundação de Amparo à Pesquisa do Estado de São Paulo—FAPESP (grants nos. 2013/07296-2 and 2019/01732-1), the Financiadora de Estudos e Projetos—FINEP, Conselho Nacional de Desenvolvimento Cientifico e Tecnológico—CNPq (grants nos. 166281/2017-4 and 426634/2018-7), and the Coordenação de Aperfeiçoamento de Pessoal de Nível Superior CAPES. J.A. acknowledges Universitat Jaume I (project UJI-B2019-30) and the Ministerio de Ciencia, Innovacio´n y Universidades (Spain) (project PGC2018094417-B-I00) for financially supporting this research. C.M. and A.S. thank the funding from the Agencia Nacional de Promoción Científica y Tecnológica—ANPCyT (Argentina) (PICT 2015-1832), the Comisión de Investigaciones Científicas de la Provincia de Buenos Aires—CICPBA (Argentina), and the Secretaría de Ciencia, Arte y Tecnología, UNCPBA (Argentina).

■ REFERENCES

(1) Alkauskas, A.; McCluskey, M. D.; Van de Walle, C. G. Tutorial: Defects in Semiconductors—Combining Experiment and Theory. *J. Appl. Phys.* **2016**, *119*, No. 181101.

(2) Park, J.-S.; Kim, S.; Xie, Z.; Walsh, A. Point Defect Engineering in Thin-Film Solar Cells. *Nat. Rev. Mater.* **2018**, *3*, 194.

(3) Bassett, L. C.; Alkauskas, A.; Exarhos, A. L.; Fu, K.-M. C. Quantum Defects by Design. *Nanophotonics* **2019**, *8*, 1867.

(4) Stoneham, A. M. *Theory of Defects in Solids: Electronic Structure of Defects in Insulators and Semiconductors*; Oxford University Press: Oxford, 2001. DOI: 10.1093/acprof:oso/9780198507802.001.0001.

(5) Baranowski, L. L.; Zawadzki, P.; Lany, S.; Toberer, E. S.; Zakutayev, A. A Review of Defects and Disorder in Multinary Tetrahedrally Bonded Semiconductors. *Semicond. Sci. Technol.* **2016**, *31*, No. 123004.

(6) Chapter V - Defects. In *CdTe and Related Compounds; Physics, Defects, Hetero- and Nano-structures, Crystal Growth, Surfaces and Applications*; Triboulet, R.; Siffert, P., Eds.; European Materials Research Society Series; Elsevier: Amsterdam, 2010; pp 169−221.

(7) Ran, C.; Xu, J.; Gao, W.; Huang, C.; Dou, S. Defects in Metal Triiodide Perovskite Materials towards High-Performance Solar Cells: Origin, Impact, Characterization, and Engineering. *Chem. Soc. Rev.* **2018**, *47*, 4581−4610.

(8) Sholl, D. S.; Lively, R. P. Defects in Metal−Organic Frameworks: Challenge or Opportunity? *J. Phys. Chem. Lett.* **2015**, *6*, 3437−3444.

(9) Chen, F.-M.; Liu, X. Advancing Biomaterials of Human Origin for Tissue Engineering. *Prog. Polym. Sci.* **2016**, *53*, 86−168.

(10) Samarth, N. Quantum Materials Discovery from a Synthesis Perspective. *Nat. Mater.* **2017**, *16*, 1068−1076.

(11) de Quilettes, D. W.; Vorpahl, S. M.; Stranks, S. D.; Nagaoka, H.; Eperon, G. E.; Ziffer, M. E.; Snaith, H. J.; Ginger, D. S. Impact of

Microstructure on Local Carrier Lifetime in Perovskite Solar Cells. *Science* **2015**, *348*, 683−686.
(12) Heo, S.; Seo, G.; Lee, Y.; Lee, D.; Seol, M.; Lee, J.; Park, J.-B.; Kim, K.; Yun, D.-J.; Kim, Y. S.; et al. Deep Level Trapped Defect Analysis in CH3NH3PbI3 Perovskite Solar Cells by Deep Level Transient Spectroscopy. *Energy Environ. Sci.* **2017**, *10*, 1128−1133.
(13) Lu, I.-T.; Bernardi, M. Using Defects to Store Energy in Materials—a Computational Study. *Sci. Rep.* **2017**, *7*, No. 3403.
(14) Hautojärvi, P.; Corbel, C. Positron Spectroscopy of Defects in Metals and Semiconductors. In *Positron Spectroscopy of Solids*; Dupasquier, A.; Mills, A. P., Jr., Eds.; IOS Press: Amsterdam, 1995.
(15) Tuomisto, F.; Makkonen, I. Defect Identification in Semiconductors with Positron Annihilation: Experiment and Theory. *Rev. Mod. Phys.* **2013**, *85*, 1583−1631.
(16) Krause-Rehberg, R.; Leipner, H. S. *Positron Annihilation in Semiconductors: Defect Studies*; Springer Science & Business Media, 1999.
(17) Tuomisto, F.; Ranki, V.; Saarinen, K.; Look, D. C. Evidence of the Zn Vacancy Acting as the Dominant Acceptor in n-Type ZnO. *Phys. Rev. Lett.* **2003**, *91*, No. 205502.
(18) Makkonen, I.; Korhonen, E.; Prozheeva, V.; Tuomisto, F. Identification of Vacancy Defect Complexes in Transparent Semiconducting Oxides ZnO, In2O3 and SnO2. *J. Phys:. Condens. Matter* **2016**, *28*, No. 224002.
(19) Brauer, G.; Anwand, W.; Skorupa, W.; Kuriplach, J.; Melikhova, O.; Moisson, C.; von Wenckstern, H.; Schmidt, H.; Lorenz, M.; Grundmann, M. Defects in Virgin and N-Implanted ZnO Single Crystals Studied by Positron Annihilation, Hall Effect, and Deep-Level Transient Spectroscopy. *Phys. Rev. B* **2006**, *74*, No. 045208.
(20) Shek, C. H.; Lai, J. K. L.; Lin, G. M. Investigation of Interface Defects in Nanocrystalline SnO2 by Positron Annihilation. *J. Phys. Chem. Solids* **1999**, *60*, 189−193.
(21) Guagliardo, P. R.; Vance, E. R.; Zhang, Z.; Davis, J.; Williams, J. F.; Samarin, S. N. Positron Annihilation Lifetime Studies of Nb-Doped TiO2, SnO2, and ZrO2. *J. Am. Ceram. Soc.* **2012**, *95*, 1727−1731.
(22) Čížek, J.; Melikhova, O.; Procházka, I.; Kuriplach, J.; Kužel, R.; Brauer, G.; Anwand, W.; Konstantinova, T. E.; Danilenko, I. A. Defect Studies of Nanocrystalline Zirconia Powders and Sintered Ceramics. *Phys. Rev. B* **2010**, *81*, 024116.
(23) Ponce, M. A.; Macchi, C.; Schipani, F.; Aldao, C. M.; Somoza, A. Mild Degradation Processes in ZnO-Based Varistors: The Role of Zn Vacancies. *Philos. Mag.* **2015**, *95*, 730−743.
(24) Macchi, C.; Ponce, M. A.; Desimone, P. M.; Aldao, C. M.; Somoza, A. Vacancy-like Defects in Nanocrystalline SnO2: Influence of the Annealing Treatment under Different Atmospheres. *Philos. Mag.* **2018**, *98*, 673−692.
(25) Saarinen, K.; Hautojärvi, P.; Corbel, C. Chapter 5 Positron Annihilation Spectroscopy of Defects in Semiconductors. In *Identification of Defects in Semiconductors*; Stavola, M. B. T.-S., Ed.; Elsevier; 1998; Vol. *51*, pp 209−285.
(26) Wang, B.-Y.; Zhang, G.-Y.; Cui, G.-W.; Xu, Y.-Y.; Liu, Y.; Xing, C.-Y. Controllable Fabrication of α-Ag2WO4 Nanorod-Clusters with Superior Simulated Sunlight Photocatalytic Performance. *Inorg. Chem. Front.* **2019**, *6*, 209−219.
(27) Longo, E.; Cavalcante, L. S.; Volanti, D. P.; Gouveia, A. F.; Longo, V. M.; Varela, J. A.; Orlandi, M. O.; Andrés, J. Direct in Situ Observation of the Electron-Driven Synthesis of Ag Filaments on α-Ag2WO4 Crystals. *Sci. Rep.* **2013**, *3*, No. 1676.
(28) Longo, E.; Volanti, D. P.; Nogueira, C.; Longo, M.; Gracia, L.; Almeida, M. A. P.; Pinheiro, A. N.; Ferrer, M. M.; Cavalcante, S.; Luis, R. W. Toward an Understanding of the Growth of Ag Filaments on α - Ag2WO4 and Their Photoluminescent Properties: A Combined Experimental and Theoretical Study. *J. Phys. Chem. C* **2014**, *118*, 1229.
(29) Sczancoski, J. C.; Maya-Johson, S.; Da Silva Pereira, W.; Longo, E.; Leite, E. R. Atomic Diffusion Induced by Electron-Beam Irradiation: An in Situ Study of Ag Structures Grown from α-Ag2WO4. *Cryst. Growth Des.* **2019**, *19*, 106−115.
(30) Lingerfelt, D. B.; Ganesh, P.; Jakowski, J.; Sumpter, B. G. Understanding Beam-Induced Electronic Excitations in Materials. *J. Chem. Theory Comput.* **2020**, *16*, 1200−1214.
(31) Zhang, Q.; Li, H.; Gan, L.; Ma, Y.; Golberg, D.; Zhai, T. In Situ Fabrication and Investigation of Nanostructures and Nanodevices with a Microscope. *Chem. Soc. Rev.* **2016**, *45*, 2694−2713.
(32) Krasheninnikov, A. V.; Nordlund, K. Ion and Electron Irradiation-Induced Effects in Nanostructured Materials. *J. Appl. Phys.* **2010**, *107*, 071301.
(33) Lin, F.; Markus, I. M.; Doeff, M. M.; Xin, H. L. Chemical and Structural Stability of Lithium-Ion Battery Electrode Materials under Electron Beam. *Sci. Rep.* **2015**, *4*, No. 5694.
(34) Wei, B.; Lu, X.; Voisard, F.; Wei, H.; Chiu, H.; Ji, Y.; Han, X.; Trudeau, M. L.; Zaghib, K.; Demopoulos, G. P.; et al. In Situ TEM Investigation of Electron Irradiation Induced Metastable States in Lithium-Ion Battery Cathodes: Li2FeSiO4 versus LiFePO4. *ACS Appl. Energy Mater.* **2018**, *1*, 3180−3189.
(35) Li, X.; Qi, J.; Zhang, Q.; Wang, Z.; Lu, S.; Zhang, Y. Investigation of Electron Beam Detection Properties of ZnO Nanowire Based Back-to-Back Double Schottky Diode. *RSC Adv.* **2014**, *4*, 12743−12747.
(36) Gonzalez-Martinez, I. G.; Bachmatiuk, A.; Bezugly, V.; Kunstmann, J.; Gemming, T.; Liu, Z.; Cuniberti, G.; Rümmeli, M. H. Electron-Beam Induced Synthesis of Nanostructures: A Review. *Nanoscale* **2016**, *8*, 11340−11362.
(37) Li, J.; Leonard Deepak, F. In Situ Generation of Sub-10 Nm Silver Nanowires under Electron Beam Irradiation in a TEM. *Chem. Commun.* **2020**, *56*, 4765−4768.
(38) Winkler, R.; Fowlkes, J. D.; Rack, P. D.; Plank, H. 3D Nanoprinting via Focused Electron Beams. *J. Appl. Phys.* **2019**, *125*, No. 210901.
(39) Assis, M.; Robeldo, T.; Foggi, C. C.; Kubo, A. M.; Mínguez-Vega, G.; Condoncillo, E.; Beltran-Mir, H.; Torres-Mendieta, R.; Andrés, J.; Oliva, M.; et al. Ag Nanoparticles/α-Ag2WO4 Composite Formed by Electron Beam and Femtosecond Irradiation as Potent Antifungal and Antitumor Agents. *Sci. Rep.* **2019**, *9*, No. 9927.
(40) Assis, M.; Cordoncillo, E.; Torres-Mendieta, R.; Beltrán-Mir, H.; Mínguez-Vega, G.; Oliveira, R.; Leite, E. R.; Foggi, C. C.; Vergani, C. E.; Longo, E.; et al. Towards the Scale-up of the Formation of Nanoparticles on α-Ag 2 WO 4 with Bactericidal Properties by Femtosecond Laser Irradiation. *Sci. Rep.* **2018**, *8*, No. 1884.
(41) Zhang, R.; Cui, H.; Yang, X.; Tang, H.; Liu, H.; Li, Y. Facile hydrothermal synthesis and photocatalytic activity of rod-like nanosized silver tungstate. *Micro Nano Lett.* **2012**, *7*, 1285−1288.
(42) Chen, H.; Xu, Y. Photoactivity and Stability of Ag2WO4 for Organic Degradation in Aqueous Suspensions. *Appl. Surf. Sci.* **2014**, *319*, 319−323.
(43) Liu, D.; Huang, W.; Li, L.; Liu, L.; Sun, X.; Liu, B.; Yang, B.; Guo, C. Experimental and Theoretical Investigation on Photocatalytic Activities of 1D Ag/Ag2WO4 Nanostructures. *Nanotechnology* **2017**, *28*, No. 385702.
(44) Longo, V. M.; De Foggi, C. C.; Ferrer, M. M.; Gouveia, A. F.; André, R. S.; Avansi, W.; Vergani, C. E.; Machado, A. L.; Andrés, J.; Cavalcante, L. S.; et al. Potentiated Electron Transference in α-Ag2WO4 Microcrystals with Ag Nanofilaments as Microbial Agent. *J. Phys. Chem. A* **2014**, *118*, 5769−5778.
(45) de Foggi, C. C.; de Oliveira, R. C.; Fabbro, M. T.; Vergani, C. E.; Andres, J.; Longo, E.; Machado, A. L. Tuning the Morphological, Optical, and Antimicrobial Properties of α-Ag2WO4 Microcrystals Using Different Solvents. *Cryst. Growth Des.* **2017**, *17*, 6239−6246.
(46) Macedo, N. G.; Machado, T. R.; Roca, R. A.; Assis, M.; Foggi, C. C.; Puerto-Belda, V.; Mínguez-Vega, G.; Rodrigues, A.; San-Miguel, M. A.; Cordoncillo, E.; et al. Tailoring the Bactericidal Activity of Ag Nanoparticles/α-Ag2WO4 Composite Induced by Electron Beam and Femtosecond Laser Irradiation: Integration of Experiment and Computational Modeling. *ACS Appl. Bio Mater.* **2019**, *2*, 824−837.
(47) De Foggi, C. C.; De Oliveira, R. C.; Assis, M.; Fabbro, M. T.; Mastelaro, V. R.; Vergani, C. E.; Gracia, L.; Andrés, J.; Longo, E.;

https://dx.doi.org/10.1021/acs.cgd.0c01417
Cryst. Growth Des. 2021, 21, 1093−1102

Machado, A. L. Unveiling the Role of β-Ag2MoO4 Microcrystals to the Improvement of Antibacterial Activity. *Mater. Sci. Eng., C* **2020**, *111*, No. 110765.
(48) da Silva Pereira, W.; Andrés, J.; Gracia, L.; San-Miguel, M. A.; da Silva, E. Z.; Longo, E.; Longo, V. M. Elucidating the Real-Time Ag Nanoparticle Growth on α-Ag2WO4 during Electron Beam Irradiation: Experimental Evidence and Theoretical Insights. *Phys. Chem. Chem. Phys.* **2015**, *17*, 5352−5359.
(49) San-Miguel, M. A.; Da Silva, E. Z.; Zanetti, S. M.; Cilense, M.; Fabbro, M. T.; Gracia, L.; Andrés, J.; Longo, E. In Situ Growth of Ag Nanoparticles on α-Ag2WO4 under Electron Irradiation: Probing the Physical Principles. *Nanotechnology* **2016**, *27*, No. 225703.
(50) Andrés, J.; Gracia, L.; Gonzalez-Navarrete, P.; Longo, V. M.; Avansi, W.; Volanti, D. P.; Ferrer, M. M.; Lemos, P. S.; La Porta, F. A.; Hernandes, A. C.; et al. Structural and Electronic Analysis of the Atomic Scale Nucleation of Ag on α-Ag2WO4 Induced by Electron Irradiation. *Sci. Rep.* **2014**, *4*, No. 5391.
(51) Longo, E.; Avansi, W.; Bettini, J.; Andrés, J.; Gracia, L. In Situ Transmission Electron Microscopy Observation of Ag Nanocrystal Evolution by Surfactant Free Electron-Driven Synthesis. *Sci. Rep.* **2016**, *6*, No. 21498.
(52) Andrés, J.; Ferrer, M. M.; Gracia, L.; Beltran, A.; Longo, V. M.; Cruvinel, G. H.; Tranquilin, R. L.; Longo, E. A Combined Experimental and Theoretical Study on the Formation of Ag Filaments on β-Ag2MoO4 Induced by Electron Irradiation. *Part. Part. Syst. Charact.* **2015**, *32*, 646−651.
(53) Lemos, P. S.; Silva, G. S.; Roca, R. A.; Assis, M.; Torre-Mendieta, R.; Beltran-Mir, H.; Minguez-Vega, G.; Cordoncillo, E.; Andrés, J.; Longo, E. Laser and Electron Beam-Induced Formation of Ag/Cr Structures on Ag2CrO4. *Phys. Chem. Chem. Phys.* **2019**, *21*, 6101−6111.
(54) Assis, M.; Carvalho de Oliveira, M.; Machado, T. R.; Macedo, N. G.; Costa, J. P. C.; Gracia, L.; Andrés, J.; Longo, E. In Situ Growth of Bi Nanoparticles on NaBiO3, δ-, and β-Bi2O3 Surfaces: Electron Irradiation and Theoretical Insights. *J. Phys. Chem. C* **2019**, *123*, 5023−5030.
(55) Assis, M.; Pontes Ribeiro, R. A.; Carvalho, M. H.; Teixeira, M. M.; Gobato, Y. G.; Prando, G. A.; Mendonça, C. R.; de Boni, L.; Aparecido de Oliveira, A. J.; Bettini, J.; et al. Unconventional Magnetization Generated from Electron Beam and Femtosecond Irradiation on α-Ag2WO4: A Quantum Chemical Investigation. *ACS Omega* **2020**, *5*, 10052−10067.
(56) Kansy, J. Microcomputer Program for Analysis of Positron Annihilation Lifetime Spectra. *Nucl. Instrum. Methods Phys. Res., Sect. A* **1996**, *374*, 235−244.
(57) Furthmüller, J.; Kresse, G. Efficiency of Ab-Initio Total Energy Calculations for Metals and Semiconductors Using a Plane-Wave Basis Set. *Comput. Mater. Sci.* **1996**, 15−50.
(58) Kresse, G.; Hafner, J. Ab Initio Molecular-Dynamics Simulation of the Liquid-Metal−Amorphous-Semiconductor Transition in Germanium. *Phys. Rev. B* **1994**, *49*, 14251−14269.
(59) Perdew, J. P.; Burke, K.; Ernzerhof, M. Generalized Gradient Approximation Made Simple. *Phys. Rev. Lett.* **1996**, *77*, 3865−3868.
(60) Kresse, G.; Joubert, D. From Ultrasoft Pseudopotentials to the Projector Augmented-Wave Method. *Phys. Rev. B* **1999**, *59*, 1758−1775.
(61) Macchi, C.; Maurizio, C.; Checchetto, R.; Mariazzi, S.; Ravelli, L.; Egger, W.; Mengucci, P.; Bazzanella, N.; Miotello, A.; Somoza, A.; et al. Niobium Aggregation and Vacancylike Defect Evolution in Nanostructured Nb-Doped Mg: Their Role in the Kinetics of the Hydride-to-Metal Phase Transformation. *Phys. Rev. B* **2012**, *85*, No. 214117.
(62) Puska, M. J.; Mäkinen, S.; Manninen, M.; Nieminen, R. M. Screening of Positrons in Semiconductors and Insulators. *Phys. Rev. B* **1989**, *39*, 7666−7679.
(63) Torsti, T.; Eirola, T.; Enkovaara, J.; Hakala, T.; Havu, P.; Havu, V.; Höynälänmaa, T.; Ignatius, J.; Lyly, M.; Makkonen, I.; et al. Three Real-Space Discretization Techniques in Electronic Structure Calculations. *Phys. Status Solidi B* **2006**, *243*, 1016−1053.
(64) Boroński, E.; Nieminen, R. M. Electron-Positron Density-Functional Theory. *Phys. Rev. B* **1986**, *34*, 3820−3831.
(65) Macedo, N. G.; Gouveia, A. F.; Roca, R. A.; Assis, M.; Gracia, L.; Andrés, J.; Leite, E. R.; Longo, E. Surfactant-Mediated Morphology and Photocatalytic Activity of α-Ag 2 WO 4 Material. *J. Phys. Chem. C* **2018**, *122*, 8667−8679.
(66) Makkonen, I.; Puska, M. J. Energetics of Positron States Trapped at Vacancies in Solids. *Phys. Rev. B* **2007**, *76*, No. 054119.
(67) Wiktor, J.; Barthe, M.-F.; Jomard, G.; Torrent, M.; Freyss, M.; Bertolus, M. Coupled experimental and DFT+U investigation of positron lifetimes in UO2. *Phys. Rev. B* **2014**, *90*, No. 184101.
(68) Cavalcante, L. S.; Almeida, M. A. P.; Avansi, W.; Tranquilin, R. L.; Longo, E.; Batista, N. C.; Mastelaro, V. R.; Li, M. S. Cluster Coordination and Photoluminescence Properties of α-Ag2WO4 Microcrystals. *Inorg. Chem.* **2012**, *51*, 10675−10687.
(69) Andres, J.; Longo, E.; Gouveia, A. F.; Gracia, L.; Oliveira, M. C. In Situ Formation of Metal Nanoparticles through Electron Beam Irradiation: Modeling Real Materials from First-Principles Calculations. *J. Mater. Sci. Eng.* **2018**, *07*, 461.
(70) Andrés, J.; Gouveia, A. F.; Gracia, L.; Longo, E.; Manzeppi Faccin, G.; da Silva, E. Z.; Pereira, D. H.; San-Miguel, M. A. Formation of Ag Nanoparticles under Electron Beam Irradiation: Atomistic Origins from First-principles Calculations. *Int. J. Quantum Chem.* **2018**, *118*, No. e25551.
(71) Tang, J.; Ye, J. Correlation of Crystal Structures and Electronic Structures and Photocatalytic Properties of the W-Containing Oxides. *J. Mater. Chem.* **2005**, *15*, 4246−4251.
(72) Tang, J.; Zou, Z.; Ye, J. Photophysical and Photocatalytic Properties of AgInW2 O8. *J. Phys. Chem. B* **2003**, *107*, 14265−14269.
(73) Sreedevi, A.; Priyanka, K. P.; Babitha, K. K.; Ganesh, S.; Varghese, T. Influence of Electron Beam Irradiation on Structural and Optical Properties of Alpha Ag2WO4. *Micron* **2016**, *88*, 1−6.
(74) Trudel, S. Unexpected Magnetism in Gold Nanostructures: Making Gold Even More Attractive. *Gold Bull.* **2011**, *44*, 3−13.
(75) Longo, V. M.; De Figueiredo, A. T.; Campos, A. B.; Espinosa, J. W. M.; Hernandes, A. C.; Taft, C. A.; Sambrano, J. R.; Varela, J. A.; Longo, E. Different Origins of Green-Light Photoluminescence Emission in Structurally Ordered and Disordered Powders of Calcium Molybdate. *J. Phys. Chem. A* **2008**, *112*, 8920−8928.
(76) Zhang, F.; Yiu, Y.; Aronson, M. C.; Wong, S. S. Exploring the Room-Temperature Synthesis and Properties of Multifunctional Doped Tungstate Nanorods. *J. Phys. Chem. C* **2008**, *112*, 14816−14824.
(77) Peters, C. A. Statistics for Analysis of Experimental Data. In *Environmental Engineering Processes Laboratory Manual*; Powers, S. E., Ed.; AEESP: Champaign, IL, 2001; pp 1−25.

https://dx.doi.org/10.1021/acs.cgd.0c01417
Cryst. Growth Des. 2021, 21, 1093−1102